Chemical Engineering Journal 426 (2021) 131843

Contents lists available at ScienceDirect

Chemical Engineering Journal

journal homepage: www.elsevier.com/locate/cej

Theory-guided design of nanoporous CuMn alloy for efficient electrocatalytic nitrogen reduction to ammonia

Yuhuan Cui [1], Anqi Dong [1], Yanbin Qu, Junyu Zhang, Ming Zhao, Zhili Wang *, Qing Jiang *

Key Laboratory of Automobile Materials, Ministry of Education, and School of Materials Science and Engineering, Jilin University, Changchun 130022, China

ARTICLE INFO

Keywords:
Nitrogen reduction reaction
Ammonia synthesis
Alloy
Nanoporous
Dealloying

ABSTRACT

Electrocatalytic nitrogen reduction reaction (NRR) is a highly attractive route for the synthesis of ammonia. However, the efficiency of the electrocatalytic NRR remains low because of the lack of effective catalyst. Here we use density functional theory (DFT) to investigate the effect of alloying Cu with Mn on NRR performance, showing that the incorporation of Mn into Cu structure can greatly improve the NRR performance. Based on the DFT results, we employ a dealloying method to prepare nanoporous CuMn (np-CuMn) alloy as the electrocatalyst for NRR. Thanks to the synergy between Cu and Mn and the nanoporous structure, the as-prepared np-CuMn alloy exhibits a high ammonia yield rate of 28.9 μg h^{-1} cm^{-2} with a Faradaic efficiency of 9.83% at −0.3 V versus reversible hydrogen electrode under ambient conditions. Both values are higher than those obtained for most of the reported noble metal catalysts under similar conditions. Our findings offer an opportunity to design high performance NRR catalyst for ammonia synthesis.

1. Introduction

Ammonia (NH_3) is essential for the production of fertilizers, pharmaceuticals, and chemicals in industry [1–3]. Recently, NH_3 has been regarded as a safe and convenient hydrogen carrier due to its high hydrogen content (17.6 wt%) and it can be easily liquefied to store and transport at room temperature [4–6]. Currently, the industrial production of NH_3 is dominated by the Haber-Bosch process. However, the Haber-Bosch process usually operates at high temperature (350–550 °C) and high pressure (150–350 atm) and emits a large amount of carbon dioxide (CO_2) [6–9]. Thus, it is highly desirable to develop an energy-efficient and environmental-friendly method to synthesize NH_3. The electrochemical N_2 reduction reaction (NRR) has been recognized as one of the most attractive routes for the synthesis of NH_3 because it utilizes renewable electricity and operates at room temperature and ambient conditions [10–13]. In recent years, tremendous efforts have been made to improve NRR performance through designing suitable electrocatalysts [14–18]. However, the electrocatalytic NRR is difficult to proceed efficiently due to the extremely strong N≡N triple bond in N_2 molecule (940.95 kJ mol^{-1}) and the occurrence of competitive reaction (hydrogen evolution reaction) in aqueous medium [19,20]. Thus, the development of highly efficient NRR catalysts for NH_3 synthesis is highly required but remains a challenge.

So far, noble metals such as Au [21], Pd [22] and their alloys [23,24] are the most active catalysts for NRR. However, the high cost and natural scarcity of noble metals severely restrict their practical applications. Thus, the development of earth-abundant metal-based catalysts for NRR is urgently required. Recently, earth-abundant metals such as Cu and Mn have been demonstrated as promising materials for NRR because they are much cheaper and more abundant than noble metals and show great potential in electrocatalyzing NRR in aqueous media [22,25–31]. For example, Chen and co-workers synthesized electron-deficient Cu nanoparticles (NPs) as catalysts for NRR, giving a NH_3 yield rate of 17.2 μg h^{-1} cm^{-2} at −0.4 V versus reversible hydrogen electrode (RHE) and a Faradaic efficiency (FE) of 6.56% at −0.3 V versus RHE [25]. Ding and co-workers applied nanoporous Pd_3Cu_1 alloy as efficient electrocatalyst for NRR which exhibited a NH_3 yield rate of 39.9 μg h^{-1} mg^{-1} [22]. Yan et al anchored $Pd_{0.2}Cu_{0.8}$ amorphous nanocluster on reduced graphene oxide as NRR catalysts, presenting a superior catalytic properity [28]. Liang and co-workers utilized the synergy of Fe and Cu atoms in confined subnano space provides significantly enhanced NRR performance [31]. Although considerable progresses in developing earth-abundant metals-based catalysts for NRR have been made, their electrocatalytic performances are still inferior to noble metal-based

* Corresponding authors.
E-mail addresses: zhiliwang@jlu.edu.cn (Z. Wang), jiangq@jlu.edu.cn (Q. Jiang).
[1] These authors contributed equally to this work.

https://doi.org/10.1016/j.cej.2021.131843
Received 17 May 2021; Received in revised form 21 July 2021; Accepted 11 August 2021
Available online 17 August 2021

catalysts. Alloying is an effective way to improve the catalytic performances of nanostructured catalysts by modulating their electronic structures and interactions with reaction intermediates [32]. For instance, bimetallic NPs with alloy structures usually exhibit much higher catalytic activities than monometallic NPs for oxygen reduction [33], CO_2 reduction [34], formic acid oxidation reactions [35], and so on. Thus, the rational design of earth-abundant metals alloy catalyst would lead to enhanced electrocatalytic performance for NRR.

Herein, we report the theory-guided design of a three-dimensional (3D) nanoporous CuMn (np-CuMn) alloy as the catalyst for NRR at room temperature under atmospheric pressure. A theoretical analysis of the reaction energetics using density functional theory (DFT) calculation shows that alloying Cu with Mn can greatly improve the NRR performance by reducing the reaction free energy of the rate determining step. According to the DFT calculation results, we synthesized a series of np-CuMn alloys with 3D interconnected nanoporous structures by a dealloying method. The 3D interconnected nanoporous structure is constructed because the metal catalyst with 3D nanoporous structure has high electric conductivity, high stability, and provides a large specific surface area with high density of stepped surface atoms as active sites for catalytic reaction [36]. Moreover, the 3D nanoporous metal synthesized by the dealloying method is a self-supported bulk material, and thus can be directly used as the electrode for electrochemical reactions without using supporting substrate and adhesive [37–40]. Benefiting from the alloying effect and nanoporous structure, the np-CuMn alloy exhibits excellent electrocatalytic performance for NRR, giving a NH_3 yield rate of 28.9 μg h^{-1} cm^{-2} with the FE of 9.83 % at −0.3 V versus RHE in 0.1 M Na_2SO_4 solution under ambient conditions.

2. Experimental section

First, the $Cu_{15}Mn_{85}$ alloy precursor was prepared by arc melting using pure Cu and pure Mn in vacuum. The as-prepared $Cu_{15}Mn_{85}$ alloy ingot was then re-melted in a quartz tube and subsequently injected onto a rotating Cu wheel under Ar atmosphere to make $Cu_{15}Mn_{85}$ alloy ribbons. Finally, the np-CuMn alloy was obtained through the selective chemical dissolution of Mn from the $Cu_{15}Mn_{85}$ alloy ribbon in 0.025 M HCl solution at room temperature for 2 h. The np-CuMn alloy catalysts with different Mn content were prepared by changing the dealloying time. The obtained np-CuMn samples were washed with ultrapure water for several times to remove residual acid and impurity ions.

3. Results and discussion

3.1. DFT calculation

The DFT calculation was firstly carried out to investigate the reaction energetics of NRR to NH_3 on Cu, Mn, and CuMn alloys with different Cu/Mn ratios. Fig. 1a shows the reaction free energies (ΔG) of NRR on different catalyst surfaces. It's clear that the rate determining step (RDS) of NRR on pure Cu, Cu_3Mn_1 and Cu_1Mn_1 is the step of first protonation of NN* to generate NNH*, whereas on Cu_1Mn_3 and pure Mn is the process of generating NH_3(g) from NH_2*. The corresponding geometric structures of intermediates during NRR on different catalyst surfaces are shown in Fig. 1b and Fig. S1. The ΔG of the RDS (ΔG_{RDS}) on pure Cu is calculated to be 1.38 eV. After alloying Cu with Mn, the ΔG_{RDS} decreases from 1.38 eV to 0.69 eV on Cu_3Mn_1 and further decreases to 0.58 eV on Cu_1Mn_1, suggesting the alloying of Cu with Mn can significantly improve the NRR activity. However, too much Mn in CuMn alloy results in the increase of ΔG_{RDS}, with which the ΔG_{RDS} on Cu_1Mn_3 alloy increases to 1.25 eV. In addition, the ΔG_{RDS} on Cu_1Mn_1 alloy is also lower than that of pure Mn (0.64 eV). As a result, the Cu_1Mn_1 alloy has the highest activity for NRR among the above metal catalysts. Fig. 1c shows the partial density of electronic states (PDOS) of nitrogen and Cu_1Mn_1 alloy before and after the nitrogen adsorption. It can be clearly seen that the obvious hybridization between catalyst and nitrogen after adsorption. Moreover, the anti-bonding orbital of nitrogen is filled after adsorption, which is a manifestation of the effective adsorption of nitrogen on the catalyst. The adsorption energies of N_2 on the Cu, Cu_3Mn_1, Cu_1Mn_1, Cu_1Mn_3 and Mn are −0.03, −0.33, −0.91, −1.23, and −0.60 eV, respectively (Fig. S2). The enhanced adsorption energies of N_2 on CuMn alloys may lead to the improved NRR activity. In addition, the adsorption energies of N_2 on top or hollow sites of Mn atoms of Cu_1Mn_1 alloy surface are greater than that on Cu atoms (Fig. S3), suggesting that the catalytic active sites of NRR in np-CuMn alloy may be Mn atoms. The Mulliken charge analysis shows that the alloying of Cu with Mn results in

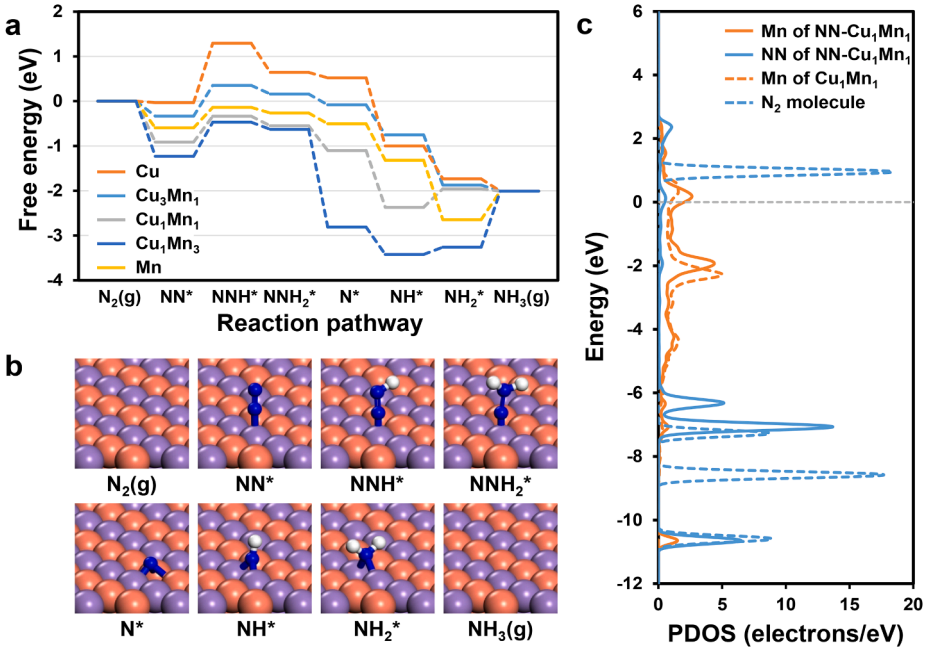

Fig. 1. Density functional theory calculations. a) Free energy diagrams of the NRR on the surfaces of Cu, Cu_3Mn_1, Cu_1Mn_1, Cu_1Mn_3 and Mn. b) The geometric structures of intermediates during NRR on Cu_1Mn_1 surface. Color code: orange, Cu; purple, Mn; blue, N; white, H; the asterisk * denotes an adsorption state. c) The partial density of electronic states of nitrogen and Cu_1Mn_1 alloy before and after the nitrogen adsorption.

charge transfer from Cu to Mn (Fig. S4). Therefore, the enhanced NRR activity of Cu_1Mn_1 alloy results from the alloying effect between Cu and Mn.

3.2. Synthesis and characterization of np-CuMn alloy

To evaluate the theoretical prediction of high performance of CuMn alloy for NRR, we prepared np-CuMn alloy catalyst by chemical dealloying $Cu_{15}Mn_{85}$ alloy in a 0.025 M HCl solution for 2 h (Fig. S5). Fig. 2a shows a representative scanning electron microscopy (SEM) image of the as-prepared np-CuMn catalyst. It can be seen that the sample has a 3D bicontinuous nanoporous structure with the pore and ligament sizes of 10 ~ 40 nm. The nanoporous structure of np-CuMn catalyst was further characterized by N_2 adsorption/desorption isotherm, which shows a typical type-IV profile (Fig. S6). The pore size mainly ranges from 10 to 40 nm. It should be noted that the ligaments with curved surfaces have a high density of atomic steps, which are chemically active for various catalytic reactions [40,41]. The high-resolution transmission electron microscopy (HRTEM) image reveals the ligament has high crystallinity, and the lattice spacing is measured to be 0.210 nm (Fig. 2b), closing to the {1 1 1} facet of face-centered cubic Cu (0.209 nm, JCPDS file: 04-0836) [42]. The atomic ratio of Cu/Mn is quantitatively determined to be 50.4/49.6 by inductively coupled plasma optical emission spectrometer (ICP-OES). The X-ray diffraction (XRD) pattern of np-CuMn (Fig. 2c) shows that the diffraction peaks at 43.3 and 50.4° can be indexed the (1 1 1) and (2 0 0) planes of a face-centered cubic structure, respectively [43]. In addition, these diffraction peaks are located between the characteristic peak of Cu (JCPDS file: 04-0836) and Mn (JCPDS file: 17-0910), demonstrating that the np-CuMn catalyst is formed as an alloy structure [44]. The energy dispersive spectrometer (EDS) mappings shown in Fig. 2d-f reveal that Cu and Mn elements are homogeneously distributed in ligament, confirming the np-CuMn is formed as an alloy structure. The X-ray photoelectron spectroscopy (XPS) spectrum of Cu 2p (932.5 eV for Cu $2p_{3/2}$ and 952.5 eV for Cu $2p_{1/2}$) shows that the surface Cu is mainly in the metallic state (Fig. S7a) [45]. The binding energy of Mn 2p3/2 can be deconvoluted into three peaks at 640.0, 641.7, and 643.7 eV, corresponding to metallic Mn, Mn^{2+} and Mn^{3+}, respectively (Fig. S7b) [46]. The presence of Mn^{2+} and Mn^{3+} in the np-CuMn alloy may be attributed to some Mn on the catalyst surface were oxidized by air during the processes of the sample preparing for XPS measurement.

3.3. Electrocatalytic NRR performance

The electrocatalytic performance of np-CuMn alloy towards NRR was explored in 0.1 M Na_2SO_4 solution under ambient condition using a gas-tight two-compartment electrochemical cell [47]. The ultra-pure N_2 (99.999%) was initially purified by Cu/SAPO trap before bubbling into the electrolyte [48,49]. Fig. 3a shows the linear sweep voltammetry (LSV) curves of the np-CuMn alloy in Ar- and N_2-saturated 0.1 M Na_2SO_4 solutions, respectively. It is clear that the current density (normalized by the geometric area) obtained in N_2-saturated electrolyte is slightly larger than that obtained in Ar-saturated electrolyte when the potential is more negative than −0.1 V versus RHE, meaning that our np-CuMn alloy can electrocatalyze the NRR under the present experimental conditions. The current density in N_2-saturated electrolyte is still greater than that in Ar-saturated electrolyte at −0.7 V versus RHE, which may be due to more gas bubbles were accumulated on the surface of catalyst in Ar-saturated electrolyte compared to that in N_2-saturated electrolyte. Similar phenomena can also be observed in the previous reports [17,50,51]. To further explore the electrocatalytic performance of np-CuMn alloy, the chronoamperometry tests were carried out with different applied potentials in the N_2-saturated electrolyte for 2 h (Fig. S8). After 2 h, the obtained electrolyte was colored with the indophenol indicator, and then characterized by the ultraviolet–visible (UV–vis) absorption. As shown in Fig. 3b, the highest absorbance peak (~655 nm) is achieved at

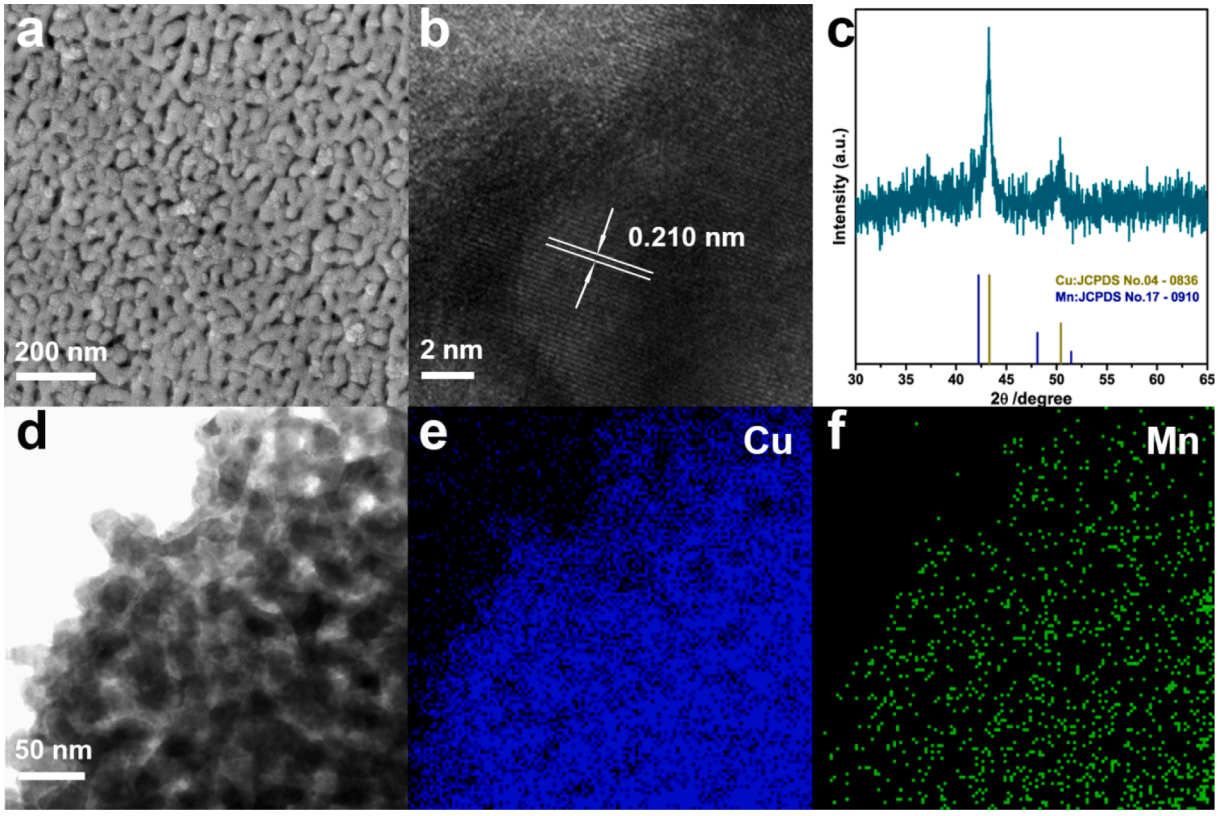

Fig. 2. Structural characterization of the np-CuMn catalyst. a) SEM image of np-CuMn. b) HRTEM image of np-CuMn. c) XRD pattern of np-CuMn. d-f) TEM image and corresponding EDS elemental mappings of np-CuMn.

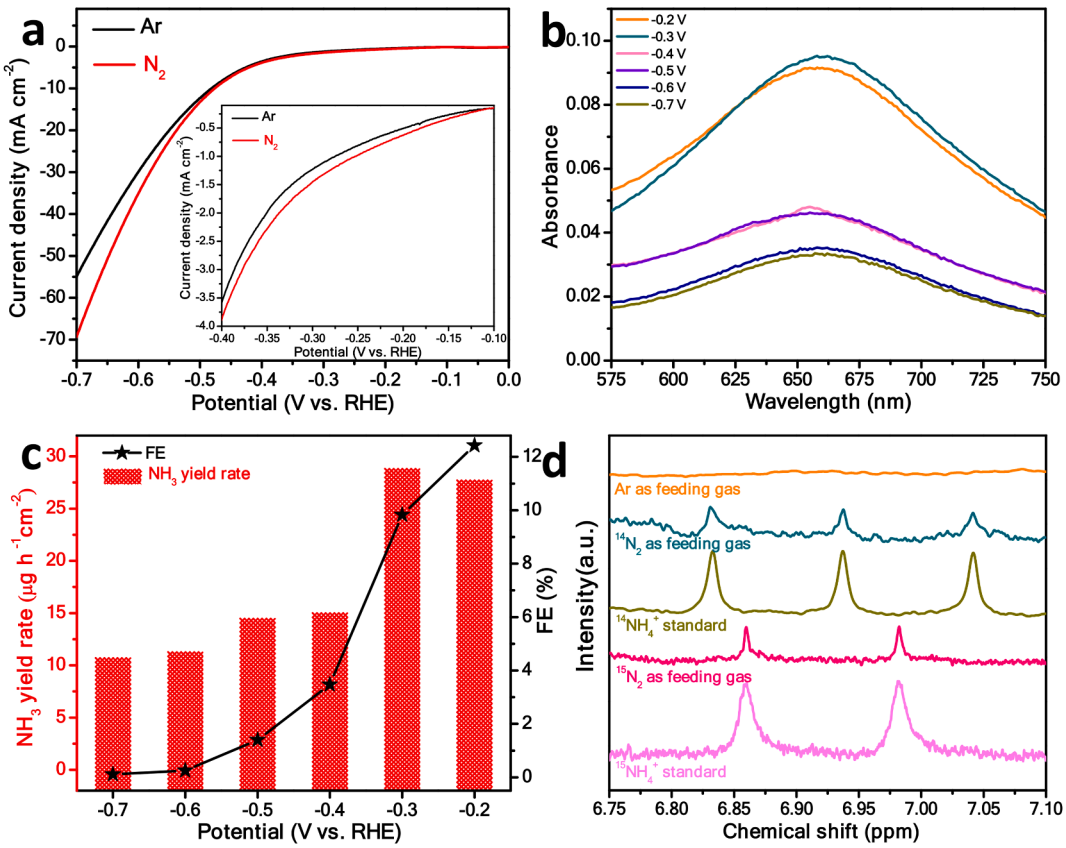

Fig. 3. NRR performance of np-CuMn alloy catalyst. a) LSV curves of np-CuMn in Ar- and N_2-saturated 0.1 M Na_2SO_4 (scan rate: 10 mV s^{-1}). b) UV–vis absorption spectra of the 0.1 M Na_2SO_4 electrolyte stained with the indophenol indicator after electrolysis at different potentials for 2 h with the np-CuMn catalyst. c) Corresponding NH_3 yield rates and FEs at various potentials. d) Isotopic labeling results from the NRR reaction at −0.3 V versus RHE using Ar, $^{14}N_2$ or $^{15}N_2$ as the feeding gas and compared to the standard $^{14}NH_4^+$ and $^{15}NH_4^+$.

−0.3 V versus RHE, suggesting that the highest NRR performance is achieved with this applied potential. The amount of generated NH_3 was quantified using the calibration curves established by the indophenol blue method (Fig. S9) [52,53]. Fig. 3c shows the NH_3 yield rate and corresponding FEs with various applied potentials. Significantly, the highest NH_3 yield rate of 28.9 μg h^{-1} cm^{-2} is achieved at −0.3 V versus RHE, and the corresponding FE is 9.83%. When the applied potentials are below −0.3 V versus RHE, both the NH_3 yield rate and FE decrease significantly due to the hydrogen evolution reaction becomes the primary process as the potential is below −0.3 V versus RHE. The FEs of H_2 over np-CuMn catalyst at different applied potentials were tested by gas chromatograph with a thermal conductivity detector. It was found that the FEs of H_2 are highly complementary to the FEs of NH_3 (Fig. S10), which suggests that the np-CuMn catalyst has certain ability to suppress hydrogen evolution reaction. In addition, only a small amount of by-product of N_2H_4 is detected (Fig. S11 and Fig. S12), indicating the excellent selectivity of our np-CuMn alloy towards the electrochemical reduction of N_2 to NH_3. It is worth noting that both the NH_3 yield rate and FE over our np-CuMn alloy are higher than that of most reported non-noble metal and noble metal catalysts under similar conditions (Table S1).

To verify the N source of the detected NH_3, a series of control experiments were carried out (Fig. S13). No apparent NH_3 is detected when using Ar as the feeding gas. With the open circuit voltage, no NH_3 is generated. The above results indicate that the detected NH_3 is produced via electrochemical reduction of N_2 rather than the contamination such as laboratory, equipment, and membrane [54–57]. To further verify the N source of obtained NH_3, the isotopic labeling experiment using $^{15}N_2$ as the feeding gas was performed [58–61]. As shown in Fig. 3d, only two peaks corresponding to $^{15}NH_4^+$ are observed when using $^{15}N_2$ as the feeding gas. On the contrary, there are three peaks corresponding to $^{14}NH_4^+$ when using $^{14}N_2$ as the feeding gas. In addition, no signal of $^{15}NH_4^+$ or $^{15}NH_4^+$ can be detected when using Ar as the feeding gas. These results further confirm that the detected NH_3 is produced via an electrochemical NRR. Moreover, the NH_3 yield rate is calculated based on the ^1H nuclear magnetic resonance spectra to be 25.5 μg h^{-1} cm^{-2}, which is consistent with result estimated by indophenol blue method (28.9 μg h^{-1} cm^{-2}) (Fig. S14).

The influence of the Mn content on the NRR performance of the np-CuMn alloy was also studied. For this end, we prepared a series of np-CuMn alloys with different Mn contents by changing the dealloying time. It was found that the Mn content can be tuned from 60.2 at.% to 49.6 at.%, 33.5 at.%, 23.4 at.% and 17.7 at.% when the dealloying time is set as 1 h, 2 h, 4 h, 6 h, and 8 h, respectively. The SEM measurement shows that the pore size increases as the dealloying time extends (Fig. 2a and Fig. S15). Fig. 4a shows the NH_3 yield rates and corresponding FEs versus the Mn content in np-CuMn alloys. It can be seen that both the NH_3 yield rate and FE increase with increasing Mn content up to 49.6 at.%. However, further increase of the Mn content in np-CuMn alloy results in the decreased NH_3 yield rate and FE. These results indicate that alloying Cu with Mn can provide a necessary synergistic effect on the electrochemical NRR, and 1:1 is the optimal ratio between Cu and Mn for this reaction. To further illustrate synergistic effect of Cu and Mn, Cu NPs, Mn NPs and bimetallic CuMn NPs were prepared by reduction of $CuSO_4$, $MnSO_4$, and $CuSO_4/MnSO_4$ mixture (molar ratio is 1:1) with $NaBH_4$ in aqueous soliton, respectively. The NRR tests show that bimetallic CuMn NPs exhibit higher NH_3 yield rate and FE than that of Cu NPs and Mn NPs (Fig. S16), suggesting the synergistic effect of Cu and Mn plays an important role in improving NRR activity. Moreover, the alloying of Mn with Cu can greatly reduce the cost of the catalyst.

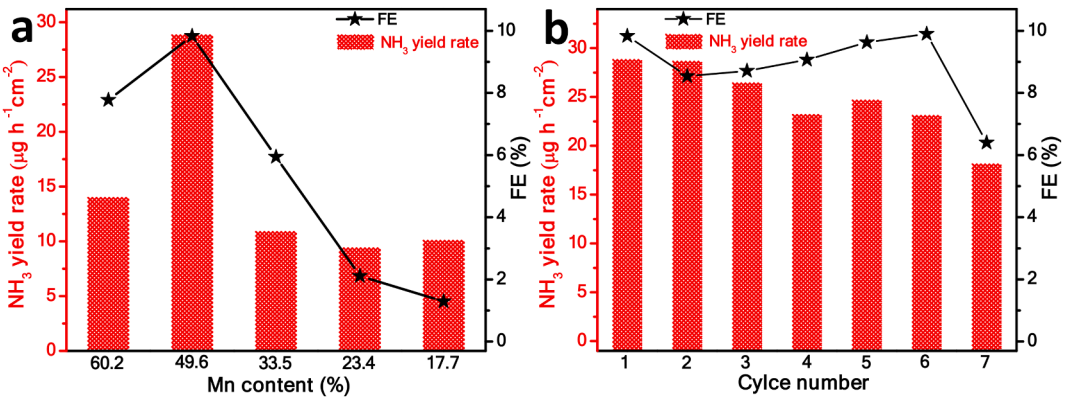

Fig. 4. NRR performance of np-CuMn alloy catalyst. a) NH_3 yield rates and FEs of np-CuMn with different Mn contents at −0.3 V versus RHE. b) Recycling tests at −0.3 V versus RHE under ambient conditions.

The pore size also affects the catalytic activity of nanoporous metal. Generally, the nanoporous metal with smaller pore size exhibits enhanced catalytic activity compared to the nanoporous metal with bigger pore size. However, the np-CuMn catalyst with bigger pore size (dealloying time 2 h) exhibits much higher NRR activity than the np-CuMn catalyst with smaller pore size (dealloying time 1 h), suggesting that the effect of pore size on NRR activity of np-CuMn catalyst is minor in comparison with that of Cu/Mn ratio.

The stability of the np-CuMn alloy towards NRR was also investigated. As shown in Fig. 4b, there is a slight decrease in the NH_3 yield rate and FE at 6th cycle. In addition, there is no noticeable morphology and size changes after six cycles (Fig. S17). There are also no obvious changes in composition, lattice spacing and crystal structure of the np-CuMn catalyst after six cycles (Fig. S18 and Fig. S19). Unfortunately, the NH_3 yield rate and FE decrease significantly at 7th cycle. Further work on enhancement of the stability of the present catalyst for the NRR is underway.

4. Conclusion

In summary, we have presented the theory-guided design of np-CuMn alloy for electrocatalytic N_2 reduction to NH_3. The theoretical investigation suggests that alloying Cu with Mn can greatly decrease the ΔG_{RDS} of NRR. As expected, the np-CuMn alloy exhibits excellent electrocatalytic performance for NRR, giving a high NH_3 yield rate of 28.9 μg h^{-1} cm^{-2} and the FE of 9.83% at −0.3 V versus RHE in 0.1 M Na_2SO_4 solution under ambient conditions, both values are higher than that of most reported no-noble metal and noble metal catalysts. Our study provides an attractive strategy for the design of high-performance NRR catalysts, and demonstrates the present np-CuMn alloy is a highly active electrocatalyst towards electrocatalytic NRR for NH_3 production.

5. Experimental section

Experimental methods and any associated references can be found in the Supporting Information.

Declaration of Competing Interest

The authors declare that they have no known competing financial interests or personal relationships that could have appeared to influence the work reported in this paper.

Acknowledgments

This work was supported by National Key R&D Program of China (2020YFB1505603) and National Natural Science Foundation of China (51901083).

Appendix A. Supplementary data

Supplementary data to this article can be found online at https://doi.org/10.1016/j.cej.2021.131843.

References

[1] V. Smil, Detonator of the population explosion, Nature 400 (6743) (1999) 415.
[2] R.F.J.e. Service, New recipe produces ammonia from air, water, and sunlight, Science 345 (6197) (2014) 610.
[3] J.-G. Chen, R.-M. Crooks, L.C. Seefeldt, K.-L. Bren, R.-M. Bullock, M.-Y. Darensbourg, P.-L. Holland, B. Hoffman, M.-J. Janik, A.-K.-J.-e. Jones, Beyond fossil fuel-driven nitrogen transformations, Science 360 (6391) (2018) 873.
[4] S. Licht, B. Cui, B. Wang, F.-F. Li, J. Lau, S. Liu, Ammonia synthesis by N_2 and steam electrolysis in molten hydroxide suspensions of nanoscale Fe_2O_3, Science 345 (6197) (2014) 637.
[5] M. Kitano, Y. Inoue, Y. Yamazaki, F. Hayashi, S. Kanbara, S. Matsuishi, T. Yokoyama, S.W. Kim, M. Hara, H.J.N.C. Hosono, Ammonia synthesis using a stable electride as an electron donor and reversible hydrogen store, Nat. Chem. 4 (11) (2012) 934–940.
[6] J. Deng, J.A. Iñiguez, C. Liu, Electrocatalytic nitrogen reduction at low temperature, Joule 2 (5) (2018) 846–856.
[7] M.A.H.J. van Kessel, D.R. Speth, M. Albertsen, P.H. Nielsen, H.J.M. Op den Camp, B. Kartal, M.S.M. Jetten, S. Lücker, Complete nitrification by a single microorganism, Nat. Chem. 528 (7583) (2015) 555–559.
[8] C. Guo, J. Ran, A. Vasileff, S.-Z. Qiao, Rational design of electrocatalysts and photo (electro)catalysts for nitrogen reduction to ammonia (NH_3) under ambient conditions, Energ. & Environ. Sci. 11 (1) (2018) 45–56.
[9] J. Wang, L. Yu, L. Hu, G. Chen, H. Xin, X. Feng, Ambient ammonia synthesis via palladium-catalyzed electrohydrogenation of dinitrogen at low overpotential, Nat. Commun. 9 (1) (2018) 1795.
[10] X. Zhu, S. Mou, P. Ling, Q. Liu, Y. Luo, G. Chen, S. Gao, X. Sun, Aqueous electrocatalytic N_2 reduction for ambient NH_3 synthesis: recent advances in catalysts developing and performances boosting, J. Mater. Chem. A 8 (2020) 1545–1556.
[11] X. Li, T. Li, Y. Ma, Q. Wei, W. Qiu, H. Guo, X. Shi, P. Zhang, A.M. Asiri, L. Chen, B. Tang, X. Sun, Boosted electrocatalytic N_2 reduction to NH_3 by defect-rich MoS_2 nanoflower, Adv. Energy Mater. 8 (30) (2018) 1801357.
[12] H. Jin, L.-Q. L, X. Liu, T. Cheng, W. Xu, S. Chen, L. Song, Y. Zheng, S.-Z. Qiao, Nitrogen vacancies on 2D layered W_2N_3: a stable and efficient active site for nitrogen reduction reaction, Adv. Mater. 31 (2019) 1902709.
[13] M.A. Légaré, G. Bélanger-Chabot, R.D. Dewhurst, E. Welz, I. Krummenacher, B. Engels, H. Braunschweig, Nitrogen fixation and reduction at boron, Science 359 (6378) (2018) 896–900.
[14] W. Tong, B. Huang, P. Wang, Q. Shao, X. Huang, Exposed facet-controlled N_2 electroreduction on distinct Pt_3Fe nanostructures of nanocubes, nanorods and nanowires, Natl. Sci. Rev. 8 (1) (2021) nwaa088.
[15] W. Cai, Y. Han, Y. Pan, X. Zhang, J. Xu, Y. Zhang, Y. Sun, S. Li, J. Lai, L. Wang, The twinned Pd nanocatalyst exhibits sustainable NRR electrocatalytic performance by promoting the desorption of NH_3, J. Mater. Chem. A 9 (23) (2021) 13483–13489.
[16] W. Cai, Y. Han, H. Li, W. Qi, J. Xu, X. Wu, H. Zhao, X. Zhang, J. Lai, L. Wang, Significantly enhanced electrocatalytic N_2 reduction to NH_3 by surface selenization with multiple functions, J. Mater. Chem. A 8 (39) (2020) 20331–20336.
[17] H. Zhao, D. Zhang, H. Li, W. Qi, X. Wu, Y. Han, W. Cai, Z. Wang, J. Lai, L. Wang, Exposure of definite palladium facets boosts electrocatalytic nitrogen fixation at low overpotential, Adv. Energy Mater. 10 (37) (2020) 2002131.
[18] Y. Deng, Z. Xiao, Z. Wang, J. Lai, X. Liu, D. Zhang, Y. Han, S. Li, W. Sun, L. Wang, The rational adjusting of proton-feeding by Pt-doped FeP/C hollow nanorod for promoting nitrogen reduction kinetics, Appl. Catal. B - Environ. 291 (2021), 120047.

[19] J. Feng, H. Pan, Electronic state optimization for electrochemical N_2 reduction reaction in aqueous solution, J. Mater. Chem. A 8 (28) (2020) 13896–13915.
[20] L. Jun, G. Zheng, One-dimensional earth-abundant nanomaterials for water-splitting electrocatalysts, Adv. Sci. 4 (2017) 1600380.
[21] S.-J. Li, D. Bao, M.-M. Shi, B.-R. Wulan, J.-M. Yan, Q. Jiang, Amorphizing of Au nanoparticles by CeOx–RGO hybrid support towards highly efficient electrocatalyst for N_2 reduction under ambient conditions, Adv. Mater. 29 (33) (2017) 1700001.
[22] F. Pang, Z. Wang, K. Zhang, J. He, W. Zhang, C. Guo, Y. Ding, Bimodal nanoporous Pd_3Cu_1 alloy with restrained hydrogen evolution for stable and high yield electrochemical nitrogen reduction, Nano Energy 58 (2019) 834–841.
[23] Q. Wang, G. Zheng, S. Hao, X. Liu, J. Zheng, Y. Wang, Z. Su, N. Xu, Y. He, L. Lei, X. Zhang, Au_1Co_1 Alloy supported on graphene oxide with enhanced performance for ambient electrolysis of nitrogen to ammonia, ACS Sustain. Chem. & Eng. 8 (1) (2020) 44–49.
[24] H. Wang, Y. Li, D. Yang, X. Qian, Z. Wang, Y. Xu, X. Li, H. Xue, L. Wang, Direct fabrication of bi-metallic PdRu nanorod assemblies for electrochemical ammonia synthesis, Nanoscale 11 (12) (2019) 5499–5505.
[25] Y.-X. Lin, S.-N. Zhang, Z.-H. Xue, J.-J. Zhang, H. Su, T.-J. Zhao, G.-Y. Zhai, X.-H. Li, M. Antonietti, J.-S. Chen, Boosting selective nitrogen reduction to ammonia on electron-deficient copper nanoparticles, Nat. Commun. 10 (1) (2019) 4380.
[26] W. Tong, B. Huang, P. Wang, L. Li, Q. Shao, X. Huang, Crystal-phase-engineered PdCu electrocatalyst for enhanced ammonia synthesis, Angew. Chem. Int. Ed. 59 (7) (2020) 2649–2653.
[27] W. Zang, T. Yang, H. Zou, S. Xi, H. Zhang, X. Liu, Z. Kou, Y. Du, Y.-P. Feng, L. Shen, L. Duan, J. Wang, S.J. Pennycook, Copper single atoms anchored in porous nitrogen-doped carbon as efficient pH-universal catalysts for the nitrogen reduction reaction, ACS Catal. 9 (11) (2019) 10166–10173.
[28] M.-M. Shi, D. Bao, S.-J. Li, B.-R. Wulan, J.-M. Yan, Q. Jiang, Anchoring PdCu amorphous nanocluster on graphene for electrochemical reduction of N_2 to NH_3 under ambient conditions in aqueous solution, Adv. Energy Mater. 8 (21) (2018) 1800124.
[29] C. Chen, X. Zhu, X. Wen, Y. Zhou, L. Zhou, H. Li, L. Tao, Q. Li, S. Du, T. Liu, D. Yan, C. Xie, Y. Zou, Y. Wang, R. Chen, J. Huo, Y. Li, J. Cheng, H. Su, X. Zhao, W. Cheng, Q. Liu, H. Lin, J. Luo, J. Chen, M. Dong, K. Cheng, C. Li, S. Wang, Coupling N_2 and CO_2 in H_2O to synthesize urea under ambient conditions, Nat. Chem. 12 (8) (2020) 717–724.
[30] H. Zhou, B. Xiong, L. Chen, J. Shi, Modulation strategies of Cu-based electrocatalysts for efficient nitrogen reduction, J. Mater. Chem. A 8 (39) (2020) 20286–20293.
[31] X. Wang, S. Qiu, J. Feng, Y. Tong, F. Zhou, Q. Li, L. Song, S. Chen, K.-H. Wu, P. Su, S. Ye, F. Hou, S.-X. Dou, H.-K. Liu, G.-Q. Lu, C. Sun, J. Liu, J. Liang, Confined Fe–Cu clusters as sub-nanometer reactors for efficiently regulating the electrochemical nitrogen reduction reaction, Adv. Mater. 32 (40) (2020) 2004382.
[32] Y. Feng, Q. Shao, J. Yujin, X. Cui, Y. Li, X. Zhu, X. Huang, Surface-modulated palladium-nickel icosahedra as high-performance non-platinum oxygen reduction electrocatalysts, Sci. Adv. 4 (2018) eaap8817.
[33] A. Holewinski, J.-C. Idrobo, S. Linic, High-performance Ag–Co alloy catalysts for electrochemical oxygen reduction, Nat. Chem. 6 (9) (2014) 828–834.
[34] X. Bai, W. Chen, C. Zhao, S. Li, Y. Song, R. Ge, W. Wei, Y. Sun, Exclusive formation of formic acid from CO_2 electroreduction by a tunable Pd-Sn alloy, Angew. Chem. Int. Ed. 56 (40) (2017) 12219–12223.
[35] Z. Xi, J. Li, D. Su, M. Muzzio, C. Yu, Q. Li, S. Sun, Stabilizing CuPd nanoparticles via CuPd coupling to $WO_{2.72}$ nanorods in electrochemical oxidation of formic acid, J. Am. Chem. Soc. 139 (42) (2017) 15191–15196.
[36] T. Fujita, P. Guan, K. McKenna, X. Lang, A. Hirata, L. Zhang, T. Tokunaga, S. Arai, Y. Yamamoto, N. Tanaka, Y. Ishikawa, N. Asao, Y. Yamamoto, J. Erlebacher, M. Chen, Atomic origins of the high catalytic activity of nanoporous gold, Nat. Mater. 11 (9) (2012) 775–780.
[37] B. Liu, J. Hou, T. Zhang, C. Xu, H. Liu, A three-dimensional multilevel nanoporous $NiCoO_2$/Ni hybrid for highly reversible electrochemical energy storage, J. Mater. Chem. A 7 (27) (2019) 16222–16230.
[38] X. Wang, M. Luo, J. Lan, M. Peng, Y. Tan, Nanoporous intermetallic Pd_3Bi for efficient electrochemical nitrogen reduction, Adv. Mater. 33 (18) (2021) 2007733.
[39] C. Xu, Q. Hao, D. Zhao, Facile fabrication of a nanoporous Si/Cu composite and its application as a high-performance anode in lithium-ion batteries, Nano Res. 9 (4) (2016) 908–916.
[40] Q. Liu, J. Hou, C. Xu, Z. Chen, R. Qin, H. Liu, TiO_2 particles wrapped onto macroporous germanium skeleton as high performance anode for lithium-ion batteries, Chem. Eng. J. 381 (2020), 122649.
[41] W. Zhang, J. He, S. Liu, W. Niu, P. Liu, Y. Zhao, F. Pang, W. Xi, M. Chen, W. Zhang, S.-S. Pang, Y. Ding, Atomic origins of high electrochemical CO_2 reduction efficiency on nanoporous gold, Nanoscale 10 (18) (2018) 8372–8376.
[42] V.L. Nguyen, B.G. Shin, D.L. Duong, S.T. Kim, D. Perello, Y.J. Lim, Q.H. Yuan, F. Ding, H.Y. Jeong, H.S. Shin, S.M. Lee, S.H. Chae, Q.A. Vu, S.H. Lee, Y.H. Lee, Seamless stitching of graphene domains on polished copper (111) foil, Adv. Mater. 27 (8) (2015) 1376–1382.
[43] X. Liu, A. Wang, L. Li, T. Zhang, C.-Y. Mou, J.-F. Lee, Structural changes of Au–Cu bimetallic catalysts in CO oxidation: in situ XRD, EPR, XANES, and FT-IR characterizations, J. Catal. 278 (2) (2011) 288–296.
[44] S. Zhang, Ö. Metin, D. Su, S. Sun, Monodisperse AgPd alloy nanoparticles and their superior catalysis for the dehydrogenation of formic acid, Angew. Chem. Int. Ed. 52 (13) (2013) 3681–3684.
[45] S. Chen, L. Brown, M. Levendorf, W. Cai, S.-Y. Ju, J. Edgeworth, X. Li, C. W. Magnuson, A. Velamakanni, R.D. Piner, J. Kang, J. Park, R.S. Ruoff, Oxidation resistance of graphene-coated Cu and Cu/Ni Alloy, ACS Nano 5 (2) (2011) 1321–1327.
[46] M.C. Biesinger, B.P. Payne, A.P. Grosvenor, L.W.M. Lau, A.R. Gerson, R.S.C. Smart, Resolving surface chemical states in XPS analysis of first row transition metals, oxides and hydroxides: Cr, Mn, Fe, Co and Ni, Appl. Surf. Sci. 257 (7) (2011) 2717–2730.
[47] L. Shi, Y. Yin, S. Wang, X. Xu, H. Wu, J. Zhang, S. Wang, H. Sun, Rigorous and reliable operations for electrocatalytic nitrogen reduction, Appl. Catal. B- Environ. 278 (2020), 119325.
[48] S.Z. Andersen, V. Čolić, S. Yang, J.A. Schwalbe, A.C. Nielander, J.M. McEnaney, K. Enemark-Rasmussen, J.G. Baker, A.R. Singh, B.A. Rohr, M.J. Statt, S.J. Blair, S. Mezzavilla, J. Kibsgaard, P.C.K. Vesborg, M. Cargnello, S.F. Bent, T.F. Jaramillo, I.E.L. Stephens, J.K. Nørskov, I. Chorkendorff, A rigorous electrochemical ammonia synthesis protocol with quantitative isotope measurements, Nature 570 (7762) (2019) 504–508.
[49] B.H.R. Suryanto, H.-L. Du, D. Wang, J. Chen, A.N. Simonov, D.R. MacFarlane, Challenges and prospects in the catalysis of electroreduction of nitrogen to ammonia, Nat. Catal. 2 (4) (2019) 290–296.
[50] L. Zeng, X. Li, S. Chen, J. Wen, W. Huang, A. Chen, Unique hollow Ni–Fe@MoS_2 nanocubes with boosted electrocatalytic activity for N_2 reduction to NH_3, J. Mater. Chem. A 8 (15) (2020) 7339–7349.
[51] S. Zhao, H.-X. Liu, Y. Qiu, S.-Q. Liu, J.-X. Diao, C.-R. Chang, R. Si, X.-H. Guo, An oxygen vacancy-rich two-dimensional Au/TiO_2 hybrid for synergistically enhanced electrochemical N_2 activation and reduction, J. Mater. Chem. A 8 (14) (2020) 6586–6596.
[52] D. Bao, Q. Zhang, F.-L. Meng, H.-X. Zhong, M.-M. Shi, Y. Zhang, J.-M. Yan, Q. Jiang, X.-B. Zhang, Electrochemical reduction of N_2 under ambient conditions for artificial N_2 fixation and renewable energy storage using N_2/NH_3 cycle, Adv. Mater. 29 (3) (2017) 1604799.
[53] L. Zhang, X. Ji, X. Ren, Y. Ma, X. Shi, Z. Tian, A.-M. Asiri, L. Chen, B. Tang, X. Sun, Electrochemical ammonia synthesis via nitrogen reduction reaction on a MoS_2 catalyst: theoretical and experimental studies, Adv. Mater. 30 (28) (2018) 1800191.
[54] J. Han, Z. Liu, Y. Ma, G. Cui, F. Xie, F. Wang, Y. Wu, S. Gao, Y. Xu, X. Sun, Ambient N_2 fixation to NH_3 at ambient conditions: using Nb_2O_5 nanofiber as a high-performance electrocatalyst, Nano Energy 52 (2018) 264–270.
[55] L. Li, C. Tang, B. Xia, H. Jin, Y. Zheng, S.-Z. Qiao, Two-dimensional Mosaic Bismuth nanosheets for highly selective ambient electrocatalytic nitrogen reduction, ACS Catal. 9 (4) (2019) 2902–2908.
[56] Y. Wang, X. Cui, J. Zhao, G. Jia, L. Gu, Q. Zhang, L. Meng, Z. Shi, L. Zheng, C. Wang, Z. Zhang, W. Zheng, Rational design of Fe–N/C hybrid for enhanced nitrogen reduction electrocatalysis under ambient conditions in aqueous solution, ACS Catal. 9 (1) (2019) 336–344.
[57] D. Zhang, H. Zhao, X. Wu, Y. Deng, Z. Wang, Y. Han, H. Li, Y. Shi, X. Chen, S. Li, J. Lai, B. Huang, L. Wang, Multi-site electrocatalysts boost pH-Universal nitrogen reduction by high-entropy alloys, Adv. Funct. Mater. 31 (2006939) (2021) 2006939.
[58] G.-F. Chen, X. Cao, S. Wu, X. Zeng, L.-X. Ding, M. Zhu, H. Wang, Ammonia electrosynthesis with high selectivity under ambient conditions via a Li^+ incorporation strategy, J. Am. Chem. Soc. 139 (29) (2017) 9771–9774.
[59] H. Cheng, L.-X. Ding, G.-F. Chen, L. Zhang, J. Xue, H. Wang, Molybdenum carbide nanodots enable efficient electrocatalytic nitrogen fixation under ambient conditions, Adv. Mater. 30 (46) (2018) 1803694.
[60] L. Zhang, L.-X. Ding, G.-F. Chen, X. Yang, H. Wang, Ammonia synthesis under ambient conditions: selective electroreduction of dinitrogen to ammonia on black phosphorus nanosheets, Angew. Chem. Int. Ed. 58 (9) (2019) 2612–2616.
[61] Y. Luo, G.-F. Chen, L. Ding, X. Chen, L.-X. Ding, H. Wang, Efficient electrocatalytic N_2 fixation with MXene under ambient conditions, Joule 3 (1) (2019) 279–289.